

Electrolyte Modulators towards Polarization Immune Lithium-Ion Batteries for Sustainable Electric Transportation

Xinru Li

University of California, Los Angeles

Pengcheng Xu

University of California, Los Angeles

Yue Tian

Shanghai Normal University

Alexis Fortini

University of California, Los Angeles

Seungho Choi

University of California, Los Angeles

Xiaoyan Liu

Shanghai Normal University

Jinhui Xu

University of California, Los Angeles

Qian Liu

Zhejiang University

Hao Bin Wu

Zhejiang University <https://orcid.org/0000-0002-0725-6442>

Gen Chen

University of California, Los Angeles

Chen Zhang

University of California, Los Angeles

Xinyi Tan

University of California, Los Angeles

Lihua Jin

University of California, Los Angeles

Qinchao Wang

Brookhaven National Laboratory

Li Shen

University of California, Los Angeles

Yunfeng Lu (✉ luucla@ucla.edu)

Article

Keywords: batteries, energy storage, electric vehicles (EV), lithium-ion batteries

Posted Date: February 25th, 2021

DOI: <https://doi.org/10.21203/rs.3.rs-265637/v1>

License:   This work is licensed under a Creative Commons Attribution 4.0 International License.

[Read Full License](#)

Electrolyte Modulators towards Polarization Immune Lithium-Ion Batteries for Sustainable Electric Transportation

Xinru Li¹, Pengcheng Xu¹, Yue Tian², Alexis Fortini¹, Seung Ho Choi¹, Xiaoyan Liu², Jinhui Xu¹, Qian Liu³, Hao Bin Wu³, Gen Chen¹, Chen Zhang¹, Xinyi Tan¹, Lihua Jin⁴, Qinchao Wang⁵, Li Shen^{1,*} and Yunfeng Lu^{1,*}

¹Department of Chemical and Biomolecular Engineering, University of California, Los Angeles, 420 Westwood Plaza, Los Angeles, California, 90095, United States.

²Education Ministry Key Lab of Resource Chemistry and Shanghai Key Laboratory of Rare Earth Functional Materials, Department of Chemistry, Shanghai Normal University, Shanghai 200234, P. R. China.

³School of Materials Science and Engineering, Zhejiang University, Hangzhou 310027, P. R. China.

⁴Department of Mechanical and Aerospace Engineering, University of California, Los Angeles, 420 Westwood Plaza, Los Angeles, California, 90095, United States.

⁵Chemistry Division, Brookhaven National Laboratory, Upton, NY 11973, United States.

*Corresponding author. Email: lishen@ucla.edu, luucla@ucla.edu

Lithium-ion batteries for electric vehicles (EV) are subject to fast charging, dynamic acceleration, and regenerative braking. However, the polarization arises from these high-rate operations and tends to deteriorate the battery performance and therefore the driving range and lifespan of EVs. Using metal organic frameworks (MOF) as electrolyte modulators

(MEM), we report herein a facile strategy for effective mitigation of polarization, where the MEM can confine anions and enrich electrolyte, affording boosted lithium-ion transference number (up to 0.76) and high ionic conductivity (up to 9 mS cm⁻¹). In addition, such MEM could implant itself into electrolyte interface, conferring the interface with low-resistance and ability to suppress concentration polarization. As a result, commercial cells with MEM deliver remarkably enhanced power output, energy efficiency, and lifespan during high rate (2C, > 3000 cycles) as well as dynamic stress tests (tripled cycle life) that mimic realistic operation of EV. This work introduces a readily implementable approach towards optimizing ion transport in electrolyte and developing polarization immune battery for power-intensive applications.

Introduction

Similar to many other electrochemical devices, lithium-ion batteries (LIB) experience polarization during cycling, which compromises their power output, energy efficiency, lifespan, and safety.¹ Generally, the polarization of batteries is associated with charge/ion transport in the active materials and electrolytes, while the way the batteries are charged/discharged is another critical factor. Polarization can commonly be cataloged into three parts: concentration polarization, activation polarization, and ohmic polarization.² Activation polarization arises from charge-transfer resistance at electrolyte-electrode interface; ohmic polarization is attributed to ionic resistance of electrolytes and electrical resistance of cell components; concentration polarization arises from ion-concentration gradient in electrolytes and active materials developed during charging and discharging.^{3, 4, 5} In a battery system, the overpotential due to ohmic polarization is dependent on the charging and discharging current, while the overpotential due to concentration polarization is dependent on both the magnitude of the current and the duration that the current was applied. A high current with a long duration will dramatically exacerbate concentration polarization.⁶

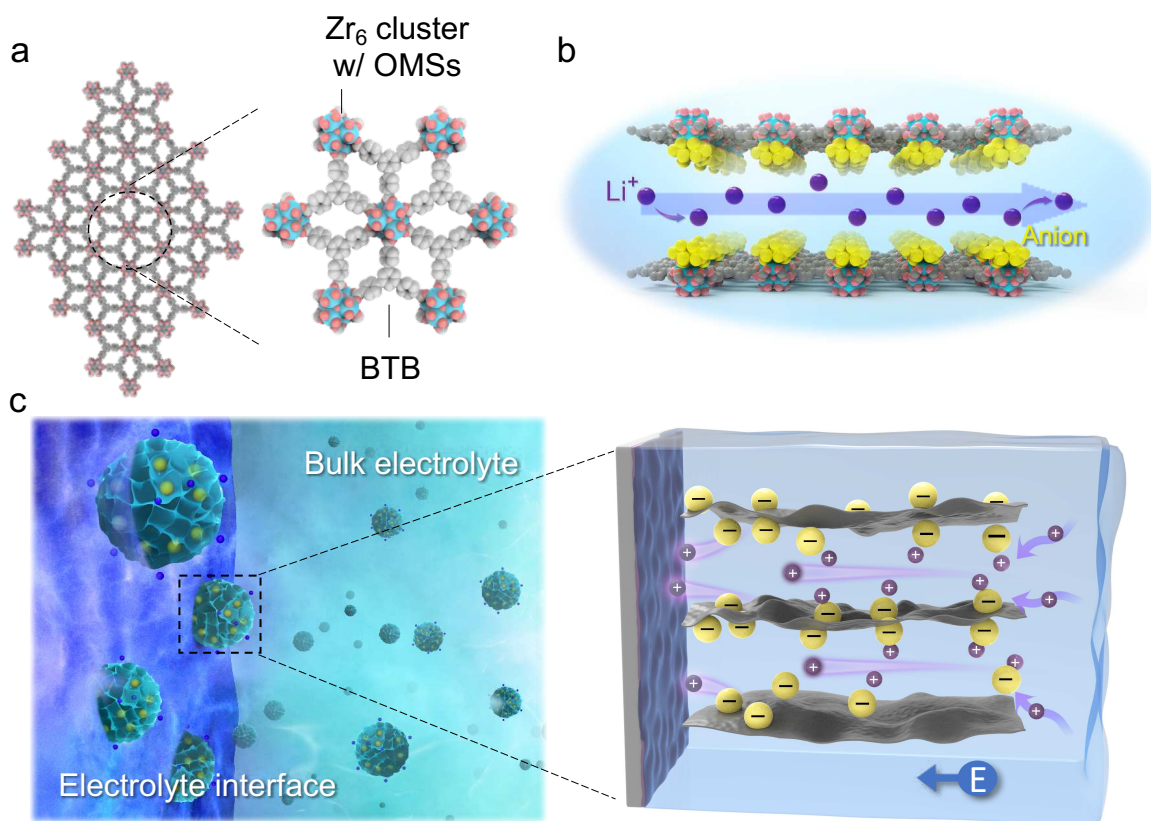
LIB designed for electric vehicle (EV) applications require fast charging, dynamic acceleration, and regenerative braking utilizing a high, dynamic current. As a result, it is important to minimize the polarization in each cell to maximize power output and durability.^{7, 8} For a standard fast-charging procedure, a 90-kWh battery pack charged to 80% of pack capacity in 15 min requires a charging power of 288 kW at 3.2 C. This rate is faster than those of many other typical LIB applications, inevitably resulting in severe polarization.⁹ During dynamic acceleration and regenerative braking, the mass transport limitations in the electrolytes (ionic resistance and concentration gradient) accounts for a significant portion of the total polarization. This contribution is further elevated when the current load is increased, especially when the load is applied for a longer time. For example, in hybrid pulse power characterization (HPPC) tests of typical LIB designed for hybrid EV, the polarization contribution from the mass transport limitations in the electrolyte grew drastically from 25% to 44% of the total polarization after 18 s of discharge at 10C, which notably hinders mass deployment of sustainable electric transportation.¹⁰

Mitigating ionic resistance and concentration polarization of electrolytes is of particular importance for LIB designed for use in electric vehicles, which is commonly achieved by increasing the ionic conductivity (σ) and/or lithium-ion transference number (t_{Li^+}) of the electrolyte. Simultaneously increasing both σ and t_{Li^+} without compromising other essential characteristics has proved to be challenging. For example, introducing co-solvents with lower viscosity to conventional liquid carbonate electrolytes could increase ion mobility and alleviate ohmic polarization.^{11, 12} However, The use of such cosolvents often deteriorates the passivation layers formed on electrodes and compromises the cycle life of batteries. Various strategies have also been explored to increase t_{Li^+} , which include adopting highly concentrated electrolytes and bulky anions, grafting anions onto polymers, and complexing anions with inorganic particles.^{13, 14} The improved t_{Li^+} , however, was often achieved at the cost of deteriorated ionic conductivity.¹⁵ ¹⁶ For example, a highly concentrated electrolyte, 7.0 M LiTFSI in dimethoxyethane (DME) and 1,3-dioxolane (DOL), provided a high t_{Li^+} of 0.73, yet with ionic conductivity 90% lower than its 1.0 M counterpart.¹⁷ Grafting anions of electrolytes on polymers resulted in electrolytes with t_{Li^+} higher than 0.8, yet with ionic conductivities two to three magnitudes lower than the liquid-electrolyte counterparts.¹⁸ In addition, various electrolyte additives have also been explored, which serve to stabilize the solid-electrolyte interface (SEI) and prolong cell lifetimes at lower rates. The use of such additives, however, tends to promote the formation of SEI films with high resistance, compromising cell performance at higher rates.^{19, 20} So it remains a daunting challenge to develop electrolyte systems with both high t_{Li^+} and σ , as well as an ability to form stable and low-resistance interface.

In this work, we report a simple yet effective solution based on an electrolyte modulator, UMCM-309a, which is a metal organic framework (MOF) constructed from hexanuclear zirconia (Zr_6) building clusters and 1,3,5-tris(4-carboxyphenyl)benzene linkers (BTB). As illustrated in Scheme 1a, UMCM-309a possesses a two-dimensional (2D) structure with an interlayer spacing of 7.01 Å and elliptical pores with a pore-window size of 7.2 Å × 12.6 Å,²¹ a size similar to that of the anion of lithium bis(trifluoromethanesulfonyl)imide (LiTFSI) (2.9 Å × 8.0 Å).²² Dispersed homogeneously in electrolytes (e.g., 1.0 M LiTFSI in DME and DOL with 1:1 volume ratio), UMCM-309a adsorbs and enriches LiTFSI from the electrolytes within the porous structure, giving rise to local high concentration. Upon dehydration of Zr_6 clusters, the formed open metal sites (OMSs) (Supplementary Fig. 1) effectively complex with anions and weaken the ion-pair interaction, leading to high t_{Li^+} and σ (Scheme 1b).

In addition, preferential complexation of anions affords UMCM-309a particles with surface charge, allowing their electrophoretic incorporation into SEI films. The incorporation of such high-conductivity moieties confers an electrolyte interface with a low resistance, as well as an ability to suppress concentration polarization in the electrolyte. Concentration polarization of electrolytes occurs especially during high-rate operations, where rapid consumption of lithium ions causes a lithium-ion deficiency near electrode surfaces. The resultant unbalanced anions are subsequently repelled from the region, resulting in a Li-salt concentration gradient and a reverse potential against the cell voltage. Unbalanced anions within such UMCM-309a-incorporated films are immobilized and create a negative electric field, which attracts surrounding lithium ions and suppresses the

concentration polarization (Scheme 1c). Combining high t_{Li^+} and σ with the ability to form robust electrolyte interfaces that have low resistance and anti-concentration-polarization capability, such MOF-based electrolyte modulators (denoted hereinafter as MEM) effectively mitigate the polarization from electrolyte and electrode-electrolyte interface.



Scheme 1 | A MOF-based-electrolyte-modulator strategy for effective mitigation of the polarization from electrolyte and electrolyte interface. a, A schematic of UMCM-309a constructed from Zr₆ clusters and BTB exhibiting a layered structure with porous networks (cyan: Zr, red: O, grey: C). **b,** Schematic of lithium-ion conduction in UMCM-309a. Complexation of OMSs with anions in the nanoporous environment afford a high t_{Li^+} and σ . **c,** A schematic illustrates the formation of an electrolyte interface incorporating UMCM-309a, affording the interface with low resistance and anti-concentration-polarization capability.

Results

Ion transport property of electrolytes with MEM. The scanning electron microscope (SEM) and transmission electron microscope (TEM) images (Figs. 1a–c) indicate that MEM has an average particle size of 0.8 μm composed of nanosheets with a thickness of ~ 7 nm (Fig. 1a, Supplementary Fig. 2) and a layer structure (d -spacing 8.3 \AA , Supplementary Fig. 3). The TEM image, along with the selected area electron diffraction (SAED) pattern, show highly ordered

lattice fringes (Fig. 1b). The topology of the Zr_6 clusters is further verified by TEM imaging in dark field mode (Fig. 1c). The distance between two adjacent clusters (20.1 Å) is consistent with reported hexagonal unit cell structure ($a = b = 20.06$ Å, space group P3m1).²³ OMSs were generated by heating the particles at 350 °C (Supplementary Fig. 4) under vacuum, which was confirmed by infrared spectroscopy. As shown in Supplementary Fig. 5, the peaks at 1417 cm^{-1} pertaining to the C=C vibrations in BTB remain unchanged, meanwhile the peak at 3420 cm^{-1} (–OH moieties) disappears after heat treatment. Meanwhile, the peaks at 484 and 635 cm^{-1} associated with the Zr_6 cluster ($Zr_6(\mu_3-O)_4(\mu_3-OH)_4$) are shifted to 496 and 655 cm^{-1} , respectively, verifying the generation of OMS after heat treatment.²⁴ The treated sample preserves the crystalline structure (Supplementary Fig. 3) and exhibits a hierarchically porous structure with a surface area of 315 $m^2 g^{-1}$ and pore volume of 0.5 $cm^3 g^{-1}$ (Supplementary Fig. 6). The micropores with a pore diameter 8.6 Å and 13.7 Å are attributed to the elliptical pores, while the meso-/macro-pores are attributed to the voids formed by stacking of the nanosheets.

MEM is readily dispersed in liquid electrolytes to form colloidal solutions, evidenced by a Tyndall effect shown in Supplementary Fig. 7. In this study, the amount of MEM added was fixed at 0.2 wt.% of electrolyte. Induction coupled plasma atomic emission spectroscopy (ICP-AES) measurement suggests that each mole of MEM enriches around 30 moles of LiTFSI in a 1.0 M LiTFSI solution, corresponding to a local LiTFSI concentration of 3.1 M (Supplementary Table 1 and Note 1). Such a high concentration is comparable to those of highly concentrated electrolytes that exhibit altered ion-pair interactions and solvation structures in comparison with their 1.0 M counterparts.^{25, 26} The ease of dispersion and enriching effect are attributable to the 2D structure and favored interactions with LiTFSI, which were confirmed by Raman and NMR spectra. Fig. 1d shows the Raman spectra of electrolytes (1.0 M LiTFSI, denoted as LFS) with and without MEM. The peaks at 741, 1136, and 1242 cm^{-1} are attributed to the vibrations related to S–N–S bending, SO_2 and CF_3 symmetric stretching of the TFSI[–] anions, respectively;²⁷ while the peaks between 2800 and 3050 cm^{-1} represent the C–H stretching of the solvent molecules. In the presence of MEM, the CF_3 and C–H peaks exhibit a minor change, while the S–N–S band appreciably shifts from 741 to 743 cm^{-1} and the SO_2 band splits into two peaks (1132/1138 cm^{-1}), confirming the interactions between the anions and the OMS.²⁴ The ¹⁹F NMR spectra of the electrolytes show an appreciable shift towards low field, confirming that the anions are consistently strongly bound to electron-withdrawing MEM,²⁸ Consistently, ⁷Li NMR spectra of the electrolytes show a subtle chemical shift (Fig. 1e).

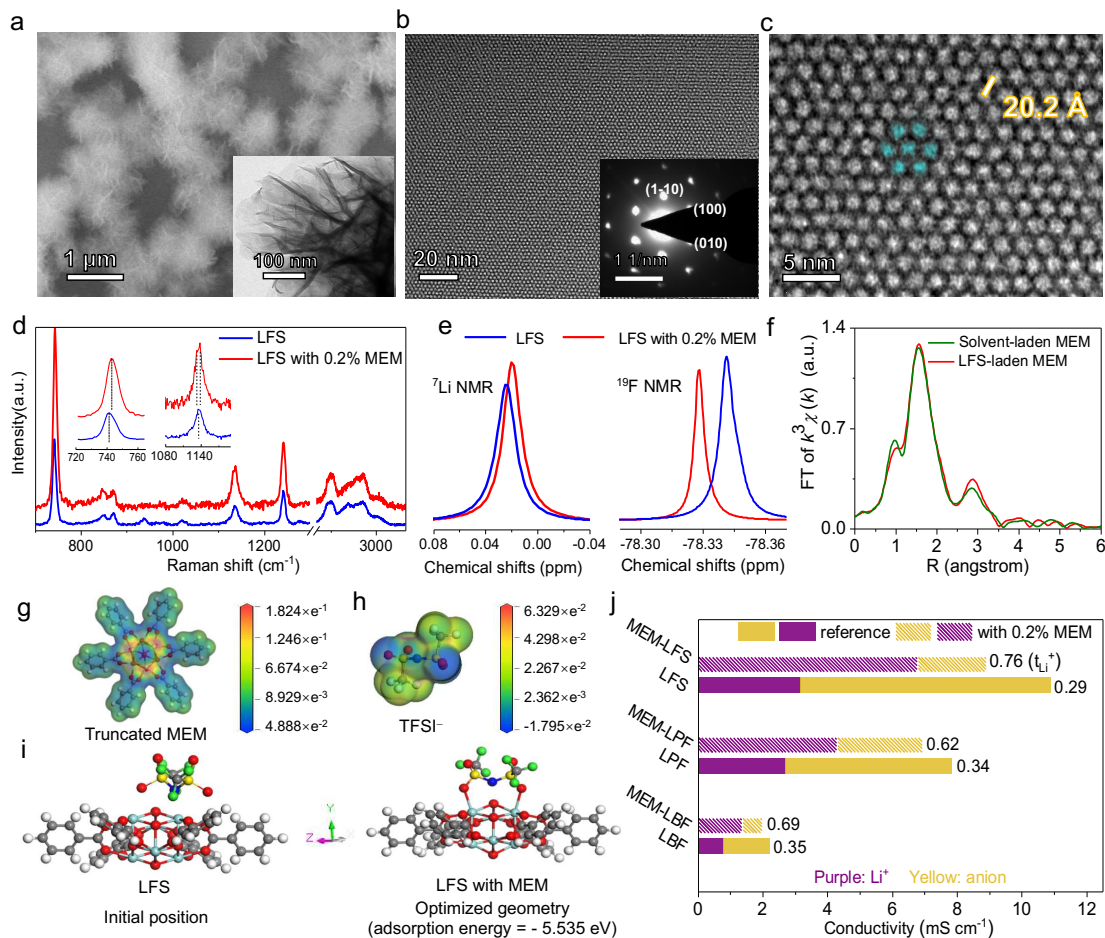


Fig. 1 | Structural characterizations of MEM and its impacts on ion transport. **a–c**, SEM (inset in **a**: TEM image) and TEM images (inset in **b**: SAED pattern) of UMCM-309a composed of nanosheets with highly ordered porous structure. **d**, Raman spectra of electrolytes with and without MEM. The inset shows the spectra for S–N–S and SO₂ vibrations. **e**, ⁷Li and ¹⁹F NMR spectra of the electrolytes with and without MEM. **f**, R-space of the extended x-ray absorption fine structure (EXAFS) spectra of MEM in DOL/DME with and without LiTFSI. **g–h**, Electrostatic potential distribution of truncated MEM (UMCM-309a) and a TFSI⁻ anion. **i**, initial and optimized adsorption configurations of a TFSI⁻ anion on a truncated MEM (cyan: Zr, red: O, grey: C, white: H, blue: N, yellow: S, green: F). **j**, Conductivity of anions and lithium ions, and t_{Li^+} of different electrolyte systems with and without MEM.

To further understand the binding configuration of TFSI⁻ on MEM, synchrotron powder x-ray adsorption spectroscopy measurement of MEM was performed in DOL/DME with and without LiTFSI. The white line of Zr K-edge remains unchanged in x-ray absorption near edge structure (XANES) spectra, indicating that the uptake of LiTFSI does not alter the valence state of the Zr₆ clusters (Supplementary Fig. 8).²⁹ Fig. 1f shows the R-space of the extended x-ray absorption fine structure (EXAFS) spectra, where the peaks at 1.6 Å and 2.9 Å are attributed to the nearest Zr–O

bonds and the distance between two adjunctive Zr atoms, respectively.^{29,30} The presence of LiTFSI increases the R-peak (2.9 Å) intensity, implying an interaction between LiTFSI and the clusters.³⁰ Figs. 1g–h show the electrostatic potential (EP) distribution of a truncated Zr₆ cluster (Supplementary Fig. 9) and a TFSI⁻ anion obtained by density functional theory (DFT). The most negative EP region of the TFSI⁻ anion is localized around the oxygen atoms of (CF₃SO₂)₂N⁻, whereas the space close to the Zr⁴⁺ centers provides the most positive EP for accommodating TFSI⁻ anions. The subsequent geometry optimization (Supplementary Table 2) suggests that the most favorable binding structure lies in where the two oxygen atoms from (CF₃SO₂)₂N⁻ bind to the nearest adjacent Zr atoms in the planar direction (Fig. 1i).

In contrast to the aforementioned strategies where an increased t_{Li^+} was achieved at the cost of a dramatically reduced ionic conductivity, adding MEM to the electrolyte system increases the t_{Li^+} from 0.29 to 0.76 and the lithium-ion conductivity, σ_{Li^+} , from 3.2 to 6.8 mS cm⁻¹, while the total ionic conductivity, σ , is only slightly reduced from 10.9 to 8.9 mS cm⁻¹ (Fig. 1j and Supplementary Figs. 10–11). Similar effects are observed in different electrolytes, including lithium hexafluorophosphate (1.0 M in ethylene carbonate and diethylene carbonate (1:1 volume ratio), denoted as LPF), and lithium tetrafluoroborate (1.0 M in propylene carbonate, denoted as LBF) (Fig. 1j, Supplementary Fig. 11), which increases the t_{Li^+} from 0.34 to 0.62 and from 0.35 to 0.69, and σ_{Li^+} from 2.7 to 4.3 mS cm⁻¹ and from 0.8 to 1.4 mS cm⁻¹, with σ lightly decreased from 7.8 to 6.9 mS cm⁻¹ and from 2.2 to 2.0 mS cm⁻¹, respectively. The results clearly suggest a general applicability of MEM for different electrolyte systems to improve their t_{Li^+} with largely retained σ . The slightly decreased value of σ is possibly ascribed to an increased ion transport tortuosity due to the presence of solid MEM.

MEM-implanted electrolyte interface with anti-polarization. Preferential complexation with anions confers MEM particles with surface charge (e.g., a *zeta* potential of around 45 mV in 0.02 M aqueous LiTFSI solution), enabling their electrophoretic incorporation into SEI films (Supplementary Fig. 12). For demonstration, symmetric Li|Li cells with and without MEM were cycled at 2 mA cm⁻² for a total capacity of 100 mAh cm⁻² (2 mAh cm⁻² per cycle). In the absence of MEM, the as-formed interface exhibits a porous and filamentous structure with a thickness of ~250 μm (Fig. 2a, Supplementary Fig. 13a); in the presence of MEM, the as-formed interphase is less dense with a thickness of ~15 μm and homogeneously incorporates the MEM particles (Figs. 2b–d, Supplementary Fig. 13b). Such an MEM-incorporated interface exhibits a high Young's modulus of 23.47 GPa measured by atomic force microscopy (AFM), well above the threshold value (6.0 GPa) for lithium-dendrite suppression (Supplementary Fig. 14).³¹ The composition of the interface was examined using x-ray photoelectron spectroscopy (XPS) (Fig. 2e), where the deconvoluted peaks at the binding energy of 688.9 eV (F 1s spectra), 399.6 eV (N 1s), 533.0 eV (O 1s), 171.7/170.3 eV (S 2p) and 293.2 eV (C 1s) are ascribable to (CF₃SO₂)₂N⁻ (TFSI⁻) anions. Several concurrent signals at 687.5/685.1 eV (F 1s), 397.5 eV (N 1s), 531.5/528.4 eV (O 1s), 168.7/163.0 eV (S 2p), and 292.9 eV (C 1s) could be assigned to C–F/LiF, Li₃N, C=O/Li₂O, –SO₃/Li–S, and –CF₂, respectively, all of which are derived from the decomposition of TFSI⁻.^{32,33} The MEM-incorporated interface shows significantly lower signals of the decomposition moieties,

indicating MEM not only aids the formation of a robust interface layer, but also prevents electrolytes from excessive decomposition.

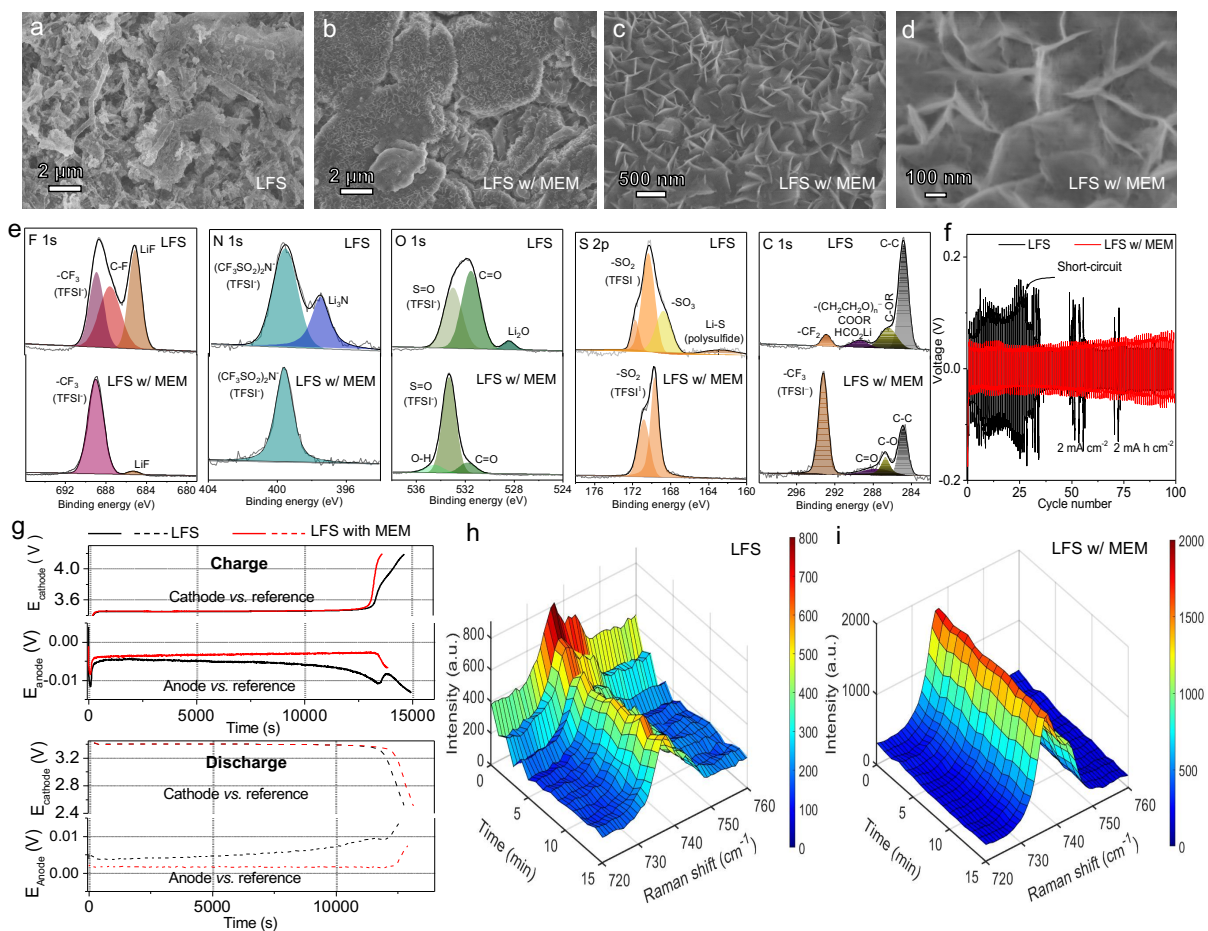


Fig. 2 | Formation of electrolyte interface with low-resistance, high modulus, and anti-concentration-polarization capability. SEM images of post-cycle lithium electrodes (25 cycles) in Li|Li cells without (a) and with (b–d) MEM. e, F 1s, N 1s, O 1s, S 2p, and C 1s spectra from XPS analysis of the cycled lithium electrodes with and without MEM. f, Galvanostatic cycling of Li|Li cells with and without MEM at an areal capacity of 2 mAh cm^{-2} and current density of 2 mA cm^{-2} . g, Cathode and anode voltage with respect to the reference electrode in a $\text{LiFePO}_4|\text{Li}|\text{Li}$ cell during cycling at a C-rate of 0.3. h–i, *In situ* Raman spectra of S–N–S vibration near the Cu electrode in the absence (h) and presence (i) of MEM during Li/Li⁺ plating at 3 mA cm^{-2} .

Fig. 2f further compares the galvanostatic cycling of symmetric Li|Li cells. The cell with MEM maintains a stable overpotential (45–55 mV) for over 100 cycles, whereas the cell without MEM displays a fluctuating and greater overpotential (e.g., 55–120 mV) with a short-circuit failure after 27 cycles. Post-cycle impedance analysis indicates that the cell with MEM has a significantly lower ohmic and interfacial resistance (Supplementary Fig. 15). To examine the effect of MEM on coulombic efficiency, Cu|Li cells were assembled and cycled at a current density of 1 mA cm^{-2} .

Lithium stripping-plating on Cu for 50 cycles exhibits an average coulombic efficiency of 96% and 78% with a voltage hysteresis of 30 mV and 65 mV at the 50th cycle, with and without MEM, respectively (Supplementary Figs. 16–17), which is consistent with mitigated decomposition of the electrolyte.

To further examine the roles of MEM in electrode-electrolyte interface, three-electrode flow cells containing a Li anode, Li reference electrode, and LiFePO₄ cathode were assembled and cycled at a C-rate of 0.3 (Fig. 2g, Supplementary Fig. 18). While the cathodes display similar voltage plateaus during cycling, the anode with MEM exhibits a more stable and significantly lower overpotential (2–3 mV vs 5–11 mV). According to the Butler-Volmer equation, the kinetic current (I) for parasitic reactions on an electrode is exponentially proportional to the overpotential (η) ($I \propto e^\eta$), implying that a 1 to 4-fold reduction of the anode overpotential observed here could lead to a 6 to 54-fold reduction of the parasitic reactions. It is worth noting that the cell without MEM shows a sudden decrease of anode overpotential near the cutoff voltage during charging, which reflects a destabilizing interface with a temporally reduced resistance. In this context, MEM not only mitigates the parasitic reactions but also serves to stabilize the interface.

The incorporation of MEM into the interface also endows a cell with unique ability to suppress concentration polarization, confirmed herein by *in situ* Raman spectroscopy collected in Cu|Li cells with and without MEM, where S–N–S vibration from TFSI⁻ anions near the Cu electrode was monitored during Li/Li⁺ plating at 3 mA cm⁻² (Supplementary Fig. 19). In the presence of MEM, the spectrum maintains ~92% of the intensity after plating for 15 min, in comparison to the case without MEM where the capacity drops by 42% shortly after plating for 3 min, confirming the resistance against concentration polarization (Figs. 2h–i).

Suppressed polarization in LiFePO₄|Li cells with MEM. The benefits of MEM in improving the power, energy output, and cycle lifespan of lithium-ion batteries was first examined in LiFePO₄|Li cells, which consist of a LiFePO₄ cathode (1 mAh cm⁻²), a Li anode (10 mAh cm⁻²), and a LiTFSI electrolyte with and without MEM, denoted as modulated and reference cell, respectively. Fig. 3a shows their galvanostatic cycling capacity at a rate of 2 C, where the reference cell retains a capacity of 142 mAh g⁻¹ for 40 cycles while the modulated cell retains a comparable capacity after 400 cycles, indicating an improved cycle lifespan. Fig 3b–e further compares the capacity (Fig. 3b), discharging time (cutoff voltage: 2.5–4.2 V) (Fig. 3c), and energy output (Fig. 3e) of the cells at different C rates, where the modulated cell well outperforms the reference cell, especially at higher C rates. At a C rate of 50, the modulated and reference cells deliver an initial power of 22.4 and 21.7 kW kg⁻¹, a discharging time of 36 and 20 s, and an energy output of 213 and 120 Wh kg⁻¹ (based on the mass of LiFePO₄), respectively. The modulated cell provides 1%, 21%, 40% and 78% improvement in energy output, in comparison with the reference cell at the C-rates of 1, 10 and 20, and 50, respectively (Fig. 3e).

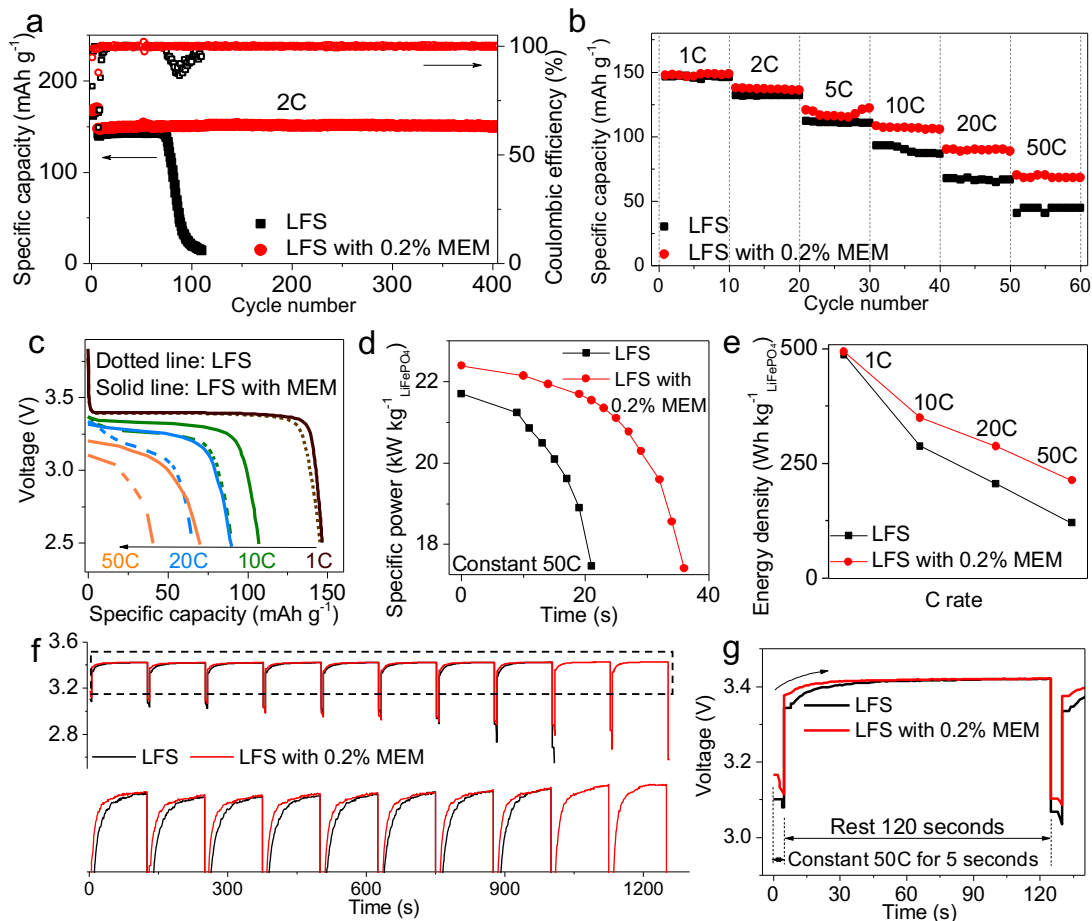


Fig. 3 | Electrochemical performance and polarization behavior of LiFePO₄/Li cells with and without MEM. Cycling stability at a C rate of 2 (initial 5 cycles at C rate of 0.5). **b–c**, Capacity (b) and discharge (c) profiles at different C-rates. **d**, Power output at a C rate of 50. **e**, Energy output at different C-rates. **f**, Cell voltage profiles with magnified view (bottom) of the pulse discharge test at a C-rate of 50. **g**, Cell voltage profiles at the first 120 s of the pulse discharge test at a C-rate of 50.

To assess the influence of concentration polarization at high rate, a pulse discharging of the cells was performed by repeatedly discharging for 5 s (at a C-rate of 50) followed by rest for 120 s. This pulse process allows the concentration polarization developed during high-rate discharging to be dissipated, manifested by an increasing cell voltage during the resting period (Fig. 3f). As expected, the modulated cell is 40 % faster (13 vs. 22 s) to reach 99 % of the final cell voltage, confirming the effectiveness of MEM in mitigating concentration polarization (Fig. 3g). Aided by the concentration relaxation during resting periods, the reference cell shows a higher improvement of energy output (115%, from 120 to 258 Wh kg⁻¹) than the modulated cell (47%, from 213 to 313 Wh kg⁻¹) (Supplementary Fig. 20), indicating that the resting periods are more favorable for the reference cell due to its severer concentration polarization. Under realistic operation of EV-use batteries, such polarization aggravated by applying high currents for long duration leads to

irreversible performance loss, which is unambiguously eased by the MEM adaptive to strenuous conditions.

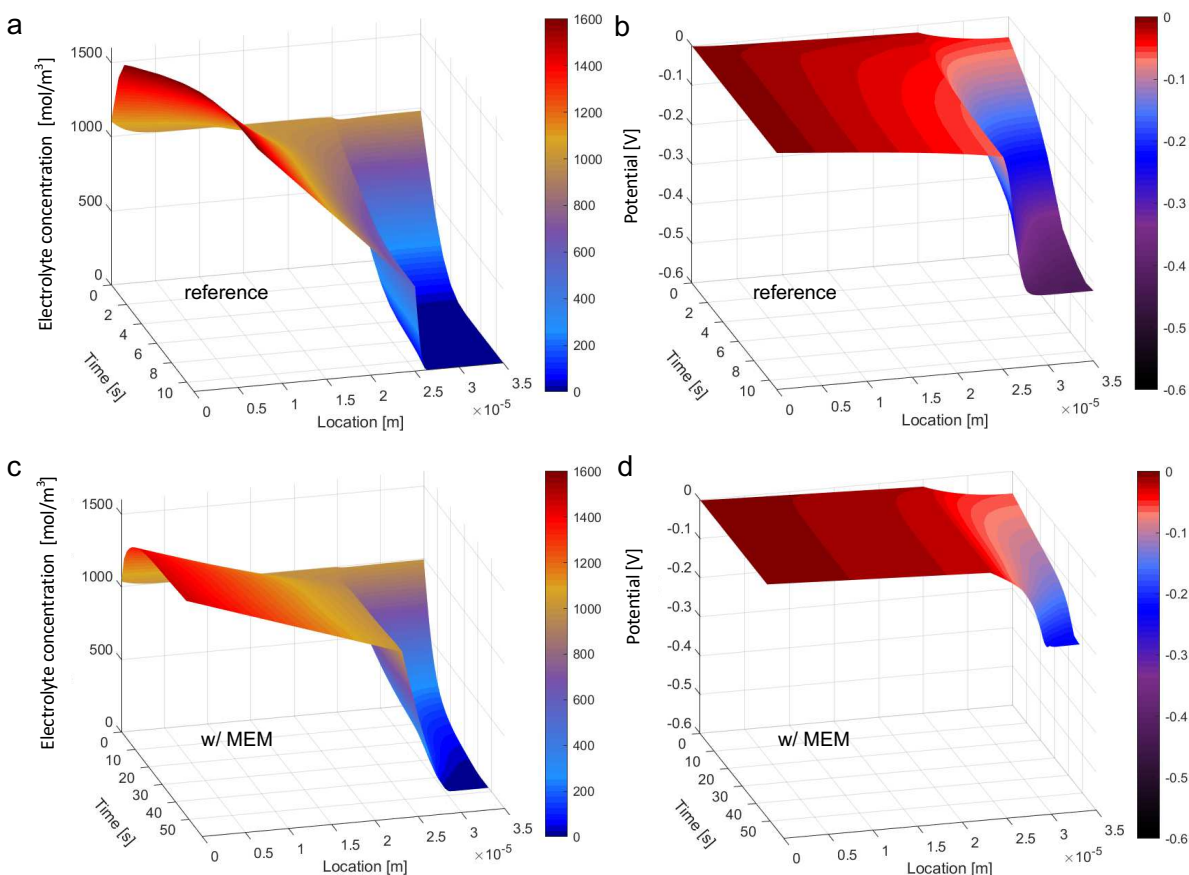


Fig. 4 | Polarization of electrolyte in simulated $\text{LiFePO}_4/\text{Li}$ cells with and without MEM. (a, c) Simulated profiles of electrolyte concentration and (b, d) overpotential during discharging at a C rate of 50.

COMSOL simulations were conducted to examine the concentration polarization in the electrolyte systems using conceptual $\text{LiFePO}_4/\text{Li}$ cells on the basis of the prototype cells (Supplementary Fig. 21), which provide discharge profiles similar to the experimental ones.³⁴ The simulation suggests that the modulated cell delivers a much higher discharge capacity (102 vs. 24 mAh g^{-1}) and longer discharging time (49 vs. 11 s) at a C rate of 50 (Supplementary Fig. 22, Supplementary Table 5), which is also consistent with experimental observation. Figs. 4a–d shows the simulated electrolyte-concentration profiles and the resultant overpotential profiles of the cells at a C rate of 50, where an overpotential of -0.23 and -0.43 V resulted from the concentration polarization is developed within 49 and 11 s for the modulated and reference cell, respectively. At a lower C rate of 20, the modulated cell develops an overpotential of -0.04 V in 178 s, whereas the reference cell still develops a much higher overpotential of -0.41 V in 96 s (Supplementary

Fig. 23). No exhaustion of the electrolyte occurs in either cells at 10C or lower (Supplementary Fig. 24). Nonetheless, the modulated cell consistently shows less polarization at the lower C-rates.

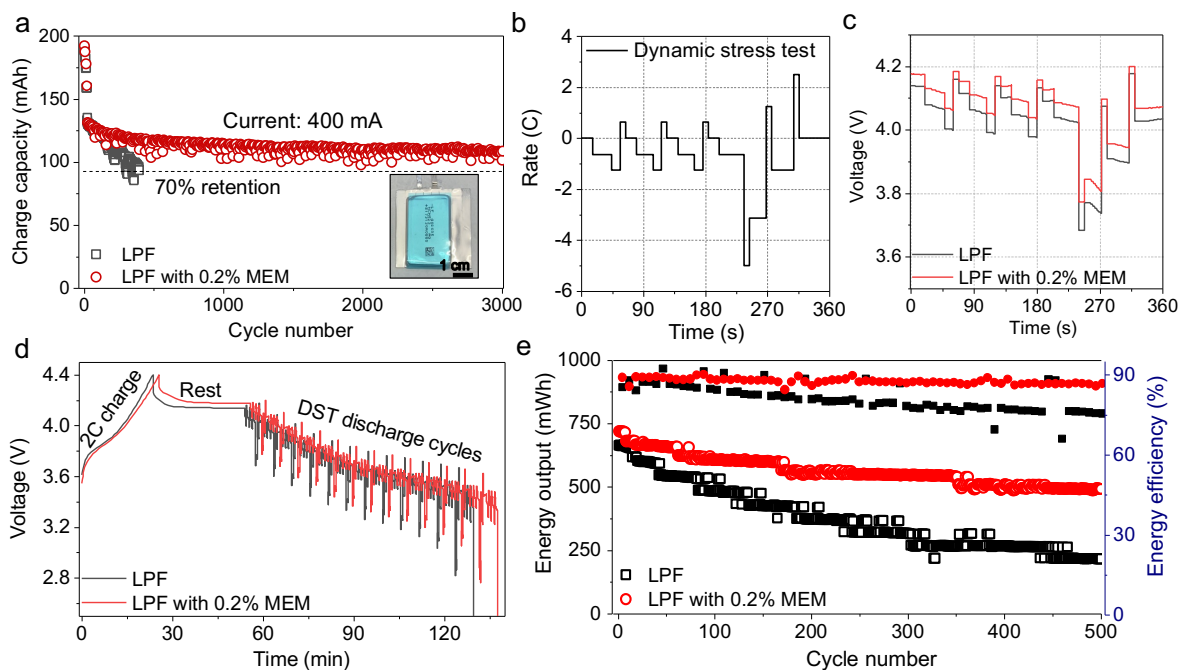


Fig. 5 | Performance of pouch cells with and without MEM in galvanostatic and dynamic stress tests. **a**, Galvanostatic cycling of commercial pouch cells at 400 mA and a voltage cutoff of 4.2 V (initial 10 cycles at 20, 30, 50, 100, 200 mA with 2 cycles for each rate). The inset shows photograph of a commercial pouch cell. **b**, Cycle protocol for a discharge process of the DST test. **c**, Voltage profiles of the first discharge segment of the DST. **d**, Voltage profiles for the first DST cycle. **e**, Cycling stability of pouch cells under DST.

Durability of MEM-boosted commercial pouch cells. The MEM was further validated in commercial pouch cells (200 mAh), which consist of a $\text{LiNi}_{0.5}\text{Co}_{0.3}\text{Mn}_{0.2}\text{O}_2$ cathode, a graphite anode, and LPF-based electrolyte, using both a galvanostatic test and dynamic stress test (DST). Under the galvanostatic test at 2C, the modulated cell maintains 70% capacity after 3000 cycles, which outperforms reference cells (70% capacity retention after 350 cycles), as well as cells with 2 wt.% fluoroethylene carbonate added to the electrolyte (70% capacity retention after 600 cycles) (Fig. 5a, Supplementary Fig. 25). The DST mimics the dynamic operation of electric vehicles (e.g., dynamic acceleration and regenerative braking), which consists of a charging-discharging pattern at different C-rates and duration illustrated in Fig. 5b. During a DST test, cells were charged to a cutoff voltage of 4.4 V under 2C, rested for 30 min, and subjected to subsequent cycles of DST until reaching a cutoff voltage of 2.5 V. Fig. 5d shows representative voltage profiles during the first DST cycle, of which the initial portion is presented in Fig. 5c. The modulated cell shows a higher open-circuit voltage (OCV) (4.17 vs. 4.14 V, ΔV 30 mV), indicating an improved charge-accepting capability. During discharging, the modulated cell delivers a higher cell voltage (e.g.,

3.77 vs. 3.68 V at 240 s, ΔV 90 mV). Note that the modulated cell shows a slightly higher voltage (e.g., 4.20 vs. 4.18 V at 312 s, ΔV 20 mV) during charging, the voltage difference, nevertheless, is comparable to that of the OCV, confirming the role of MEM in mitigating polarization of the cells during dynamic operation conditions.

Fig. 5e further compares the energy output and energy efficiency of the cells under DST. The modulated cell delivered an energy output of 719 and 492 mWh in the 1st and 500th test cycle with 70% energy-output retention, outperforming the reference cell that delivers an energy output of 664 and 216 mWh in the 1st and 500th cycle with 32 % energy-output retention, respectively. In terms of energy efficiency, the modulated cell also provided a higher efficiency of 89 % and 87% in the 1st and 500th cycle with a retention rate of 98%, also outperforming the reference cell that gave an efficiency of 89% and 76 % in the 1st and 500th cycle with a much lower retention rate of 85%. The ability of MEM to dramatically improve the power and energy output, energy efficiency, and cycle life under the dynamic operation conditions of LIB is of particular importance for electric vehicle applications.

Discussion

It is noted that, under actual conditions of electric vehicles, polarization due to mass transport of electrolyte (concentration polarization and ohmic polarization due to the ionic resistance) could account for nearly half of the total polarization. Moreover, prevailing concentration polarization could lead to electrolyte depletion and intensified side reactions, which further aggravate activation polarization and shorten the lifespan of batteries. Mitigating the polarization of electrolyte, in this context, is vitally important towards vehicle-use batteries and electrification of transportation fleet.

However, the most current strategies fail to alleviate those polarizations in a synergistic manner. This work presents an all-around solution using 2D MOF as MEM. In terms of ion-transport in electrolyte, adding a low concentration of MEM (0.2 wt.%) to commercial electrolytes effectively boosts their t_{Li^+} (up to 0.76) while largely preserves their ionic conductivity (up to 9 mS cm⁻¹). In terms of electrolyte interface, we demonstrated that, if anions can be immobilized while Li-ions are allowed to freely translocate within electrolyte interface, a local electric field will be established to effectively recruit surrounding Li-ions and suppress concentration polarization. This electric-field strategy is critical for metal batteries (e.g., lithium metal batteries), where concentration polarization has been a main cause of dendrite growth. In terms of efficacy, MEM dramatically improves the power output, energy efficiency, and cycle lifespan of commercial pouch cells under strenuous conditions mimicked those of electric vehicles.

In summary, this work reports a MEM strategy to effectively mitigate the polarization from the electrolyte and electrode-electrolyte interface, which successfully address a long-standing issue that LIB could suffer from drastic performance deterioration under strenuous operations. Such MEM binds anions, enriches neighboring electrolyte and ensures dominant Li-ion conduction. As heavy-load exhausts electrolyte close to the interface, MEM could preferentially transport Li-ions to replenish the shortage and thus mitigate the polarization, imparting excellent interfacial stability and exceptional longevity. In commercial pouch cells, MEM dramatically prolongs the cell

lifespan from 350 to beyond 3000 cycles (2C). Under dynamic stress tests that adapt to vehicle operations, the cell with MEM could offer boosted power output (faster acceleration), improved energy output (extended driving range), increased energy efficiency and reduced energy decay (longer service life). This easy-to-implement strategy creates a new route towards polarization immune LIB by overcoming the mass transport limitations, which boosts the sustainable adoption and growth of EV.

Methods

Synthesis of UMCM-309a The UMCM-309a was synthesized according to a reported hydrothermal approach.²³ ZrCl₄ (0.37 mmol) and BTB (0.25 mmol) were dissolved in 30 mL of dimethylformamide (DMF) and 10.75 mL of 12 M HCl. The mixture was sealed in a Teflon lined autoclave and heated at 120 °C for 2 days. After cooling to room temperature, the UMCM-309a powders collected by centrifugation were successively washed by DMF for 3 times and by acetone over 3 days. The sample was dried at 120 °C overnight and further heated at 350 °C (under vacuum) for 12 h to thermally activate the UMCM-309a. The activated UMCM-309a was dispersed into liquid electrolytes (LFS/LPF from BASF, home-made LBF) at a 0.2 wt.% of the electrolytes (in an Argon-filled glove box). The resulting colloidal suspensions were ultrasonicated for 30 min and magnetically stirred overnight.

In situ Raman. A Raman spectrometer (Dilor, SuperLabram II), which is equipped with a 633 nm laser and a custom-made Cu|Li cell with a quartz window, was used to analyze the concentration of electrolyte in vicinity of the Cu electrode during Li⁺ plating at a current density of 3 mA cm⁻². Cells with 5 mL of electrolyte were assembled and sealed in a glove box. The electrodes (1 cm² in size) were fixed with a distance of 0.3 cm, a laser beam was focused at a fixed position (0.1 cm) from the Cu electrode, and Raman spectra were collected at a time interval of 1 min during the plating.

Electrochemical characterizations. Ionic conductivity of electrolytes with MEM was measured using a home-made electrolyte cell, where two identical titanium plates (1×1 cm⁻²) served as blocking electrodes. The ionic resistance was estimated by the extrapolated interception of the Nyquist plots with the real axis. The determination of t_{Li^+} was performed through the combination of EIS technique and potentiostatic polarization. Li|Li cells were polarized by a constant voltage bias of 20 mV (ΔV) for 1 h, during which the initial current (I_0) was monitored until reaching the steady-state current (I_{SS}), and the interfacial resistance was recorded by the EIS before (R_0) and after (R_{SS}) the potentiostatic polarization. The t_{Li^+} thereby could be calculated with the following expression: $t_{Li^+} = I_{SS} (\Delta V / I_0 R_0) / (I_0 (\Delta V / I_{SS} R_{SS}))$.³⁵ The cyclic voltammetry (CV) tests (Biologic VMP3) were conducted in SS|Li cells at scan rate of 1 mV s⁻¹ between -0.2 V and 5 V (vs. Li/Li⁺). The conductivity of LFS and LPF were acquired directly from the manufacturer datasheets.

LiFePO₄|Li porotype cells. LiFePO₄ cathodes were prepared by mixing LiFePO₄ (Shenzhen Dynanonic Co), super P, and polyvinylidene fluoride (PVDF) at a weight ratio of 94:3:3 in N-methyl-2-pyrrolidone (NMP). The resulting slurries were uniformly coated on carbon-coated Al

foils and dried in a vacuum oven at 120 °C for 24 h. The half-cell (LiFePO₄|Li) tests were performed with coin-type cells (CR 2032), a polyethylene-based separator (Celgard, 25 μm), thin Li foil (40 μm), and 60 μL of LFS-based electrolyte. Three-electrode flow cell (LiFePO₄|Li|Li) tests were carried out in a commercial air-tight split cell (MTI) (see schematic in Supplementary Fig. 18), which was assembled with a LiFePO₄ (12 mm), Li disk (14 mm) and Li foil as cathode, anode, and reference electrode, respectively. The reference electrode was inserted between the cathode and anode with separations of glass fiber membranes (Whatman, GF/C) and 2 mL of LFS-based electrolyte. All cells were fabricated in an Argon-filled glove box (O₂/H₂O < 1 ppm). The galvanostatic cycling of cells was performed between 2.5 to 4.2 V (vs. Li/Li⁺) with a 1C rate equal to 150 mA g⁻¹. Before the pulsed 50C discharge tests, the LiFePO₄|Li cells were charged to 4.2V at a low rate of 0.3C. The loading levels of LiFePO₄ for the three-electrode and rate tests were at 2-3 mg cm⁻² and a higher ~6 mg cm⁻² loading was applied for the long-term cycle tests (2C).

Pouch-type full cell tests. Dry (without electrolyte) and sealed LiNi_{0.5}Co_{0.3}Mn_{0.2}O₂|graphite pouch cells (200 mAh, balanced at 4.4 V) were purchased from Li-FUN technology, where the single side loadings of the cathodes were 14.5 mg cm⁻². The cells were opened, dried, filled with electrolyte (LPF-based), and sealed in glove box. Afterwards the cells were rested for 24 h, charged under 10 mA (0.05 C) to 3.5 V, and then held at 3.5 V until the current dropped below 0.05C. The activated cells were degassed and replenished with electrolyte in glove box. The total added volume of electrolyte was 0.85 mL. The conventional DST protocol was scaled to C-rates, where 5C discharge corresponds to the maximum peak power output. Voltage cutoffs of 4.2 V and 4.4 V were applied for galvanostatic (400 mA) and DST cycles, respectively. All electrochemical tests were conducted at ambient temperature (25 °C) and minor temperature fluctuations may have occurred due to facility management.

DFT calculations. All computations were performed by means of spin-polarized DFT methods using the DMol³ code.^{36,37} The generalized gradient approximation (GGA) and the Perdew-Burke-Ernzerhof (PBE) exchange-correlation functional were employed.³⁸ The *van der Waals* interactions were described using the empirical correction in the Grimme scheme, and the density functional semicore pseudopotential (DSPP) was adopted for the relativistic effects of transition metal atoms, in which the core electrons are replaced by a single effective potential with some degree of relativistic corrections introduced into the core.^{39,40} The double numerical plus (DNP) polarization was chosen as the basis set for other elements.³⁶ Self-consistent field (SCF) calculations were performed with a convergence criterion of 10⁻⁶ au on the total energy of electronic computations. To ensure high quality results, the real-space global orbital cutoff radius was chosen as high as 5.3 Å and thermal smearing with a width of 0.01 Ha was applied to the orbital occupation to speed up the convergence. Since the simplified UMCM-309a cluster structure was placed in a length of 60 Å box cube, a Monkhorst-Pack k-point sampling of 1×1×1 mesh was used in this calculation.⁴¹

Finite element simulation. LiFePO₄|Li conceptual cells were modeled in COMSOL Multiphysics[®] using the Batteries and Fuel Cells Module on the basis of a pseudo two-dimensional (P2D) model developed by Newman et al.^{6,34} The geometry setup consists of a lithium metal anode surface at $x = 0$, a separator domain from $x = 0$ to $x = 25 \mu\text{m}$, a porous LiFePO₄ positive

electrode domain from $x = 25 \mu\text{m}$ to $x = 35 \mu\text{m}$, and a current collector surface at $x = 35 \mu\text{m}$. The geometry is discretized into finite points along the x -axis, and for the porous electrode domain, an extra pseudo dimension, r , is used to describe the transport of solid lithium through the active material particles. Butler-Volmer kinetics are used to describe the flux of lithium ions at the particle surfaces. The independent variables, including the lithium-ion concentration and potential in the electrolyte, as well as the solid lithium concentration and electric potential in the active material particles, are solved for at each nodal point using the transport equations and boundary conditions described in Supplementary Information Section 3.1. All of the constant parameters used in the model equations are listed in the Supplementary Table 3, and the assumptions that were used to build the model are listed in Supplementary Table 4.

References

1. Liu Y, Zhu Y, Cui Y. Challenges and opportunities towards fast-charging battery materials. *Nature Energy* **4**, 540-550 (2019).
2. Arora P, Doyle M, Gozdz AS, White RE, Newman J. Comparison between computer simulations and experimental data for high-rate discharges of plastic lithium-ion batteries. *Journal of Power Sources* **88**, 219-231 (2000).
3. Krachkovskiy SA, Bazak JD, Werhun P, Balcom BJ, Halalay IC, Goward GR. Visualization of Steady-State Ionic Concentration Profiles Formed in Electrolytes during Li-Ion Battery Operation and Determination of Mass-Transport Properties by in Situ Magnetic Resonance Imaging. *Journal of the American Chemical Society* **138**, 7992-7999 (2016).
4. Takamatsu D, Yoneyama A, Asari Y, Hirano T. Quantitative Visualization of Salt Concentration Distributions in Lithium-Ion Battery Electrolytes during Battery Operation Using X-ray Phase Imaging. *Journal of the American Chemical Society* **140**, 1608-1611 (2018).
5. Klett M, *et al.* Quantifying Mass Transport during Polarization in a Li Ion Battery Electrolyte by in Situ ^7Li NMR Imaging. *Journal of the American Chemical Society* **134**, 14654-14657 (2012).
6. Doyle M, Fuller TF, Newman J. Modeling of Galvanostatic Charge and Discharge of the Lithium/Polymer/Insertion Cell. *Journal of The Electrochemical Society* **140**, 1526-1533 (1993).
7. Cano ZP, *et al.* Batteries and fuel cells for emerging electric vehicle markets. *Nature Energy* **3**, 279-289 (2018).
8. Keil P, Jossen A. Impact of Dynamic Driving Loads and Regenerative Braking on the Aging of Lithium-Ion Batteries in Electric Vehicles. *Journal of The Electrochemical Society* **164**, A3081-A3092 (2017).

9. Logan ER, Dahn JR. Electrolyte Design for Fast-Charging Li-Ion Batteries. *Trends in Chemistry* **2**, 354-366 (2020).
10. Nyman A, Zavalis TG, Elger R, Behm Mr, Lindbergh Gr. Analysis of the Polarization in a Li-Ion Battery Cell by Numerical Simulations. *Journal of The Electrochemical Society* **157**, A1236 (2010).
11. Cho Y-G, Kim Y-S, Sung D-G, Seo M-S, Song H-K. Nitrile-assistant eutectic electrolytes for cryogenic operation of lithium ion batteries at fast charges and discharges. *Energy & Environmental Science* **7**, 1737-1743 (2014).
12. Hilbig P, Ibing L, Winter M, Cekic-Laskovic I. Butyronitrile-Based Electrolytes for Fast Charging of Lithium-Ion Batteries. *Energies* **12**, (2019).
13. Diederichsen KM, McShane EJ, McCloskey BD. Promising Routes to a High Li⁺ Transference Number Electrolyte for Lithium Ion Batteries. *ACS Energy Letters* **2**, 2563-2575 (2017).
14. Lagadec MF, Zahn R, Wood V. Characterization and performance evaluation of lithium-ion battery separators. *Nature Energy* **4**, 16-25 (2019).
15. Popovic J, Höfler D, Melchior JP, Münchinger A, List B, Maier J. High Lithium Transference Number Electrolytes Containing Tetratriflypropene's Lithium Salt. *The Journal of Physical Chemistry Letters* **9**, 5116-5120 (2018).
16. Borodin O, *et al.* Liquid Structure with Nano-Heterogeneity Promotes Cationic Transport in Concentrated Electrolytes. *ACS Nano* **11**, 10462-10471 (2017).
17. Suo L, Hu Y-S, Li H, Armand M, Chen L. A new class of Solvent-in-Salt electrolyte for high-energy rechargeable metallic lithium batteries. *Nature Communications* **4**, 1481 (2013).
18. Song J, Lee H, Choo M-J, Park J-K, Kim H-T. Ionomer-Liquid Electrolyte Hybrid Ionic Conductor for High Cycling Stability of Lithium Metal Electrodes. *Scientific Reports* **5**, 14458 (2015).
19. Liu QQ, Ma L, Du CY, Dahn JR. Effects of the LiPO₂F₂ additive on unwanted lithium plating in lithium-ion cells. *Electrochimica Acta* **263**, 237-248 (2018).
20. Liu QQ, Xiong DJ, Petibon R, Du CY, Dahn JR. Gas Evolution during Unwanted Lithium Plating in Li-Ion Cells with EC-Based or EC-Free Electrolytes. *Journal of The Electrochemical Society* **163**, A3010-A3015 (2016).
21. Wang R, Wang Z, Xu Y, Dai F, Zhang L, Sun D. Porous Zirconium Metal–Organic Framework

- Constructed from 2D \rightarrow 3D Interpenetration Based on a 3,6-Connected kgd Net. *Inorganic Chemistry* **53**, 7086–7088 (2014).
22. Largeot C, Portet C, Chmiola J, Taberna P-L, Gogotsi Y, Simon P. Relation between the Ion Size and Pore Size for an Electric Double-Layer Capacitor. *Journal of the American Chemical Society* **130**, 2730–2731 (2008).
 23. Ma J, Wong-Foy AG, Matzger AJ. The Role of Modulators in Controlling Layer Spacings in a Tritopic Linker Based Zirconium 2D Microporous Coordination Polymer. *Inorganic Chemistry* **54**, 4591–4593 (2015).
 24. Shen L, *et al.* Creating Lithium-Ion Electrolytes with Biomimetic Ionic Channels in Metal–Organic Frameworks. *Advanced Materials* **30**, 1707476 (2018).
 25. Yamada Y, *et al.* Unusual Stability of Acetonitrile-Based Superconcentrated Electrolytes for Fast-Charging Lithium-Ion Batteries. *Journal of the American Chemical Society* **136**, 5039–5046 (2014).
 26. Yamada Y, Yaegashi M, Abe T, Yamada A. A superconcentrated ether electrolyte for fast-charging Li-ion batteries. *Chemical Communications* **49**, 11194–11196 (2013).
 27. Suo L, Zheng F, Hu Y-S, Chen L. FT-Raman spectroscopy study of solvent-in-salt electrolytes. *Chinese Physics B* **25**, 016101 (2016).
 28. Qiao B, Leverick GM, Zhao W, Flood AH, Johnson JA, Shao-Horn Y. Supramolecular Regulation of Anions Enhances Conductivity and Transference Number of Lithium in Liquid Electrolytes. *Journal of the American Chemical Society* **140**, 10932–10936 (2018).
 29. Zhang J-Y, *et al.* Adsorption of Uranyl ions on Amine-functionalization of MIL-101(Cr) Nanoparticles by a Facile Coordination-based Post-synthetic strategy and X-ray Absorption Spectroscopy Studies. *Scientific Reports* **5**, 13514 (2015).
 30. Sang X, *et al.* Ionic liquid accelerates the crystallization of Zr-based metal–organic frameworks. *Nature Communications* **8**, 175 (2017).
 31. Monroe C, Newman J. The Impact of Elastic Deformation on Deposition Kinetics at Lithium/Polymer Interfaces. *Journal of The Electrochemical Society* **152**, A396 (2005).
 32. Diao Y, Xie K, Xiong S, Hong X. Insights into Li-S Battery Cathode Capacity Fading Mechanisms: Irreversible Oxidation of Active Mass during Cycling. *Journal of The Electrochemical Society* **159**, A1816–A1821 (2012).

33. Alvarado J, *et al.* Bisalt ether electrolytes: a pathway towards lithium metal batteries with Ni-rich cathodes. *Energy & Environmental Science* **12**, 780-794 (2019).
34. Cai L, White RE. Mathematical modeling of a lithium ion battery with thermal effects in COMSOL Inc. Multiphysics (MP) software. *Journal of Power Sources* **196**, 5985-5989 (2011).
35. Zugmann S, Fleischmann M, Amereller M, Gschwind RM, Wiemhöfer HD, Gores HJ. Measurement of transference numbers for lithium ion electrolytes via four different methods, a comparative study. *Electrochimica Acta* **56**, 3926-3933 (2011).
36. Delley B. An all-electron numerical method for solving the local density functional for polyatomic molecules. *The Journal of Chemical Physics* **92**, 508-517 (1990).
37. Delley B. From molecules to solids with the DMol3 approach. *The Journal of Chemical Physics* **113**, 7756-7764 (2000).
38. Perdew JP, Burke K, Ernzerhof M. Generalized Gradient Approximation Made Simple. *Physical Review Letters* **77**, 3865-3868 (1996).
39. Grimme S. Semiempirical GGA-type density functional constructed with a long-range dispersion correction. *Journal of Computational Chemistry* **27**, 1787-1799 (2006).
40. Delley B. Hardness conserving semilocal pseudopotentials. *Physical Review B* **66**, 155125 (2002).
41. Monkhorst HJ, Pack JD. Special points for Brillouin-zone integrations. *Physical Review B* **13**, 5188-5192 (1976).

Acknowledgements

This work is under support of UCLA-HK Center for Graphene Technology and Energy Storage. XAS experiments were carried out at beamlines 7-BM (QAS) of the National Synchrotron Light Source II, a U.S. Department of Energy (DOE) Office of Science User Facility operated for the DOE Office of Science by Brookhaven National Laboratory under Contract No. DE-SC0012704. We like to thank Dr. Yunyao Xu from Columbia University for the NMR analysis and Dr. Renwei Liu from Shimadzu Company for the AFM testing.

Author contributions

X.R.L., Y.T., L.S., G.C. and J.X. performed the materials synthesis and characterization. X.R.L., S.H.C, L.S., X.Y.L., and X.L. carried out the evaluations on electrolyte properties. P.X., A.F. and

L.J conducted the COMSOL simulations. Q.W. conducted the XAS experiments. H.B.W and Q.L. conducted the DFT calculation. X.R.L., L.S., C.Z, X.T and Y.T. tested and analyzed the electrochemical performances. X.R.L., L.S., and Y.L. co-wrote the manuscript. Y.L. conceived the idea and supervised the project.

Competing interests

The authors declare no competing interests.

Figures

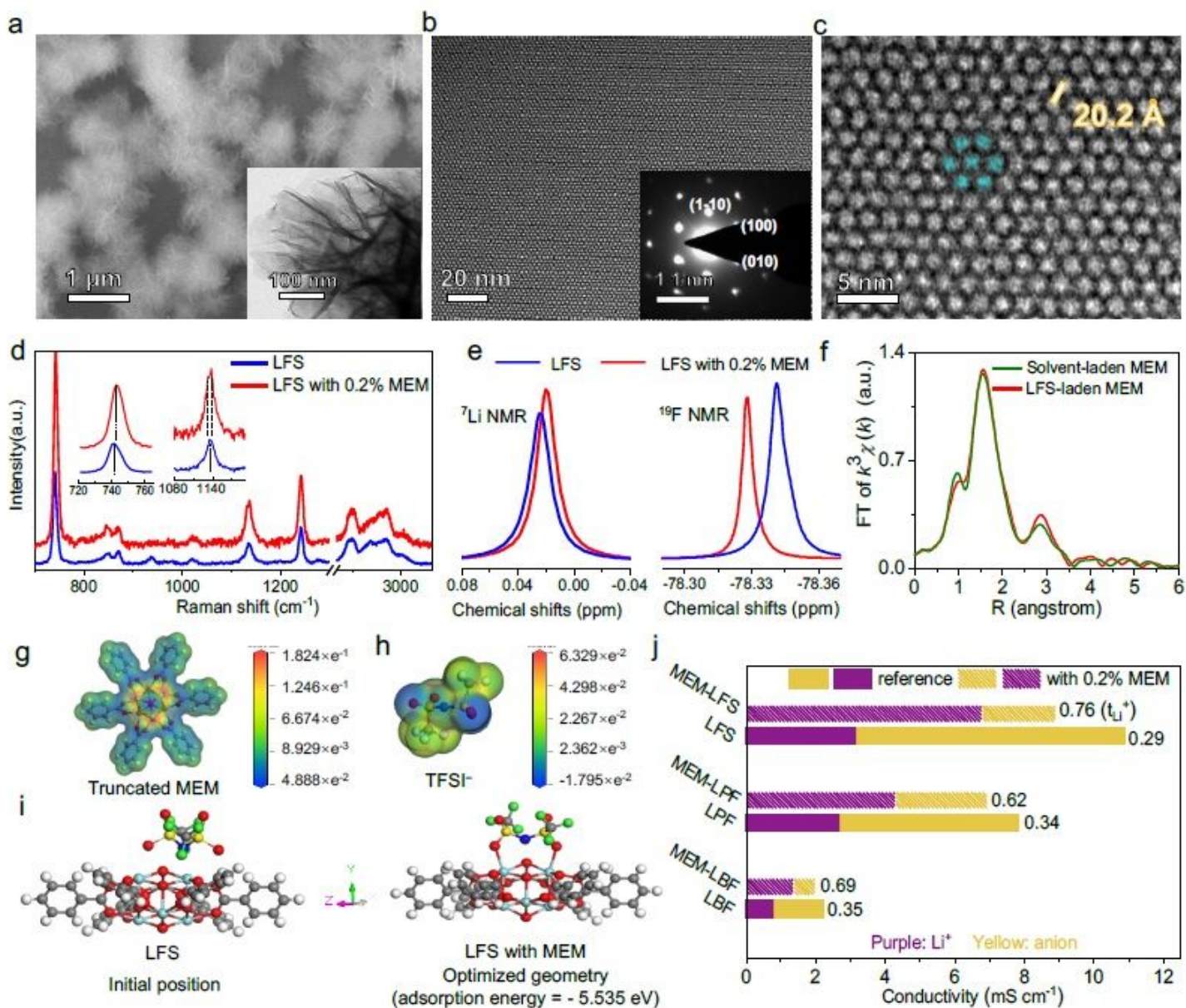


Figure 1

Structural characterizations of MEM and its impacts on ion transport. a–c, SEM (inset in a: TEM image) and TEM images (inset in b: SAED pattern) of UCMC-309a composed of nanosheets with highly ordered porous structure. d, Raman spectra of electrolytes with and without MEM. The inset shows the spectra for S–N–S and SO₂ vibrations. e, ⁷Li and ¹⁹F NMR spectra of the electrolytes with and without MEM. f, R-space of the extended x-ray absorption fine structure (EXAFS) spectra of MEM in DOL/DME with and without LiTFSI. g–h, Electrostatic potential distribution of truncated MEM (UMCM-309a) and a TFSI⁻ anion. i, initial and optimized adsorption configurations of a TFSI⁻ anion on a truncated MEM (cyan: Zr, red: O, grey: C, white: H, blue: N, yellow: S, green: F). j, Conductivity of anions and lithium ions, and t_{Li^+} of different electrolyte systems with and without MEM.

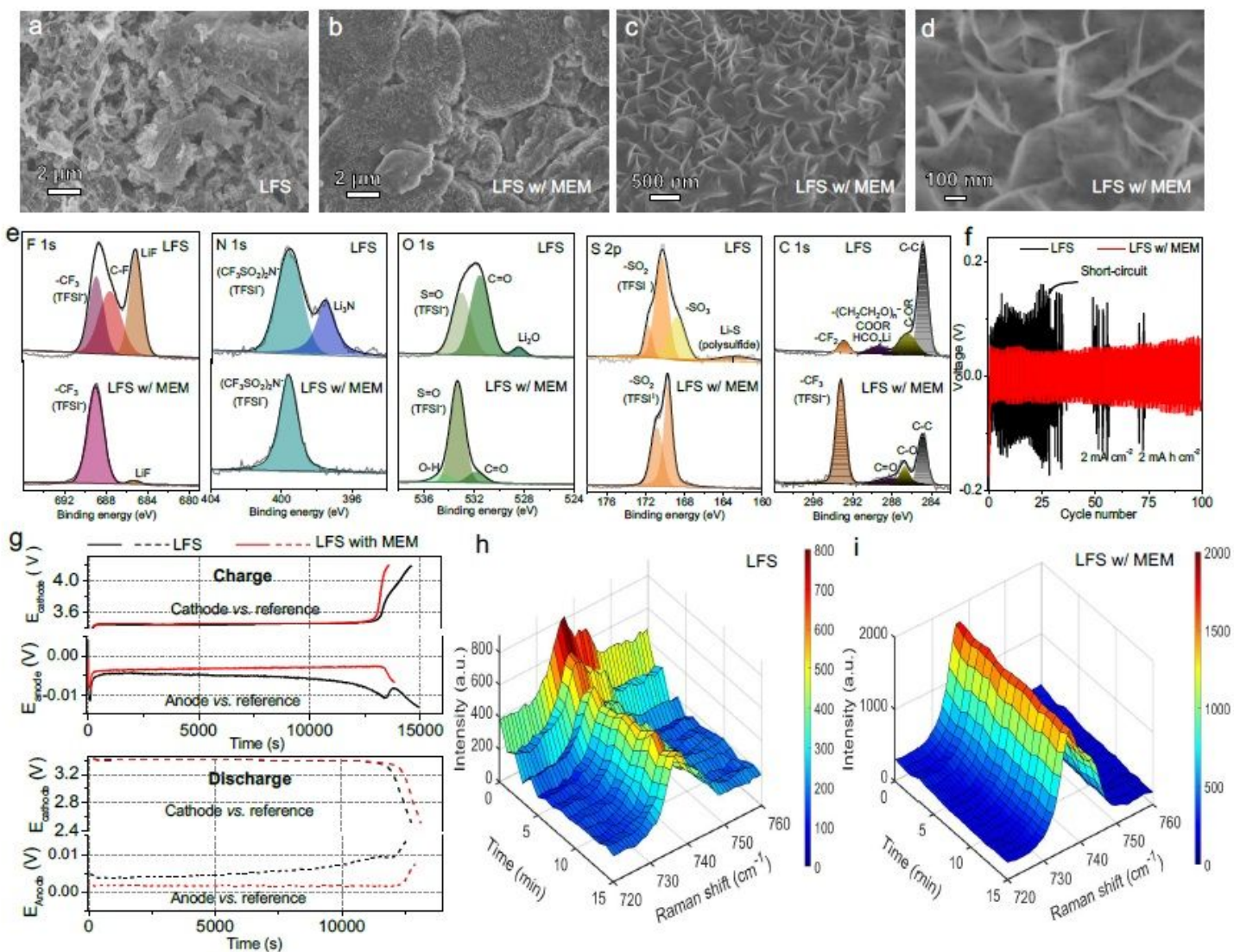


Figure 2

Formation of electrolyte interface with low-resistance, high modulus, and anticoncentration-polarization capability. SEM images of post-cycle lithium electrodes (25 cycles) in Li|Li cells without (a) and with (b-d) MEM. e, F 1s, N 1s, O 1s, S 2p, and C 1s spectra from XPS analysis of the cycled lithium electrodes with and without MEM. f, Galvanostatic cycling of Li|Li cells with and without MEM at an areal capacity of 2 mAh cm^{-2} and current density of 2 mA cm^{-2} . g, Cathode and anode voltage with respect to the reference electrode in a $\text{LiFePO}_4|\text{Li}|/\text{Li}$ cell during cycling at a C-rate of 0.3. h-i, In situ Raman spectra of S-N-S vibration near the Cu electrode in the absence (h) and presence (i) of MEM during Li/Li⁺ plating at 3 mA cm^{-2} .

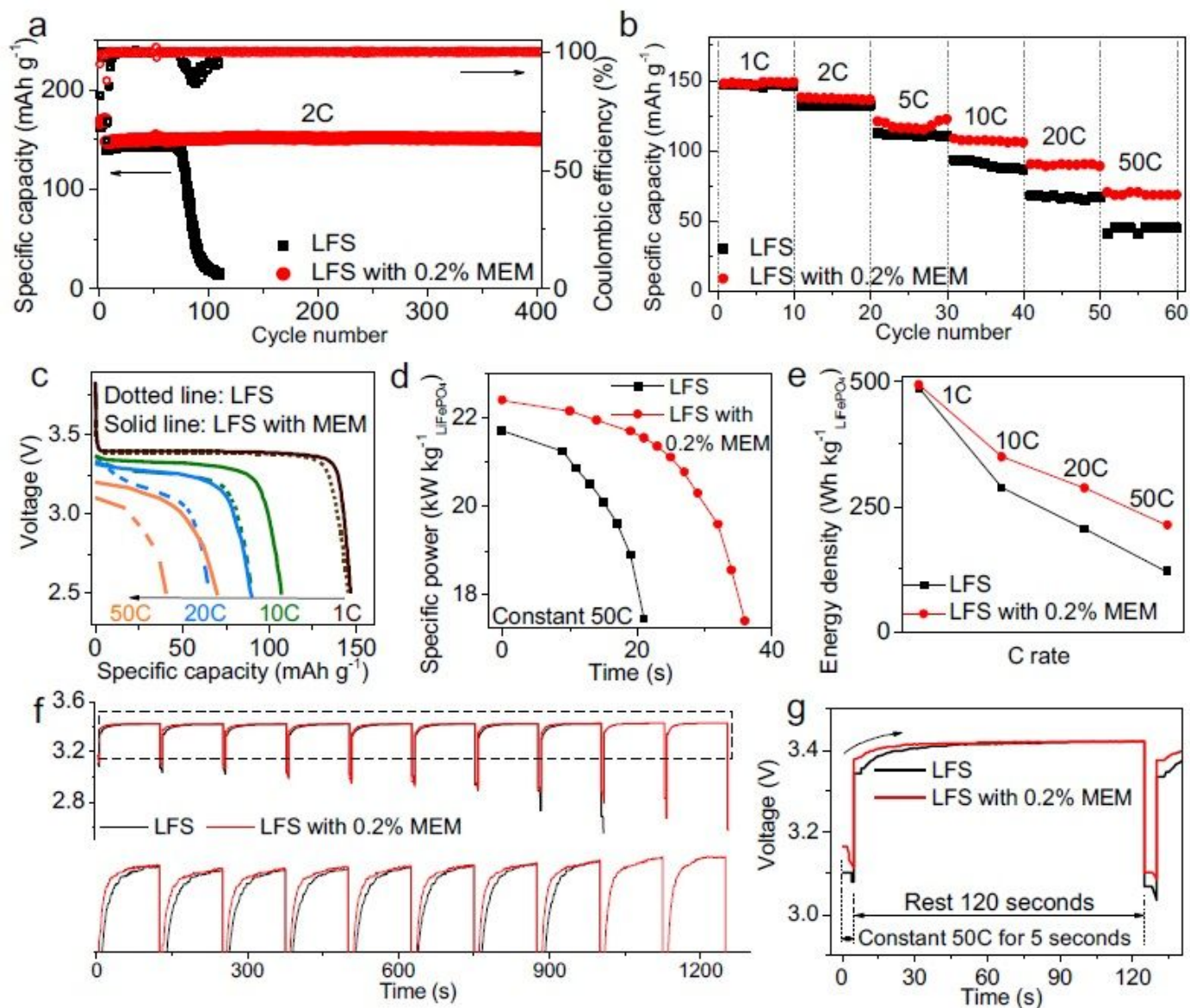


Figure 3

Electrochemical performance and polarization behavior of LiFePO₄|Li cells with and without MEM. Cycling stability at a C rate of 2 (initial 5 cycles at C rate of 0.5). b–c, Capacity (b) and discharge (c) profiles at different C-rates. d, Power output at a C rate of 50. e, Energy output at different C-rates. f, Cell voltage profiles with magnified view (bottom) of the pulse discharge test at a C-rate of 50. g, Cell voltage profiles at the first 120 s of the pulse discharge test at a C-rate of 50.

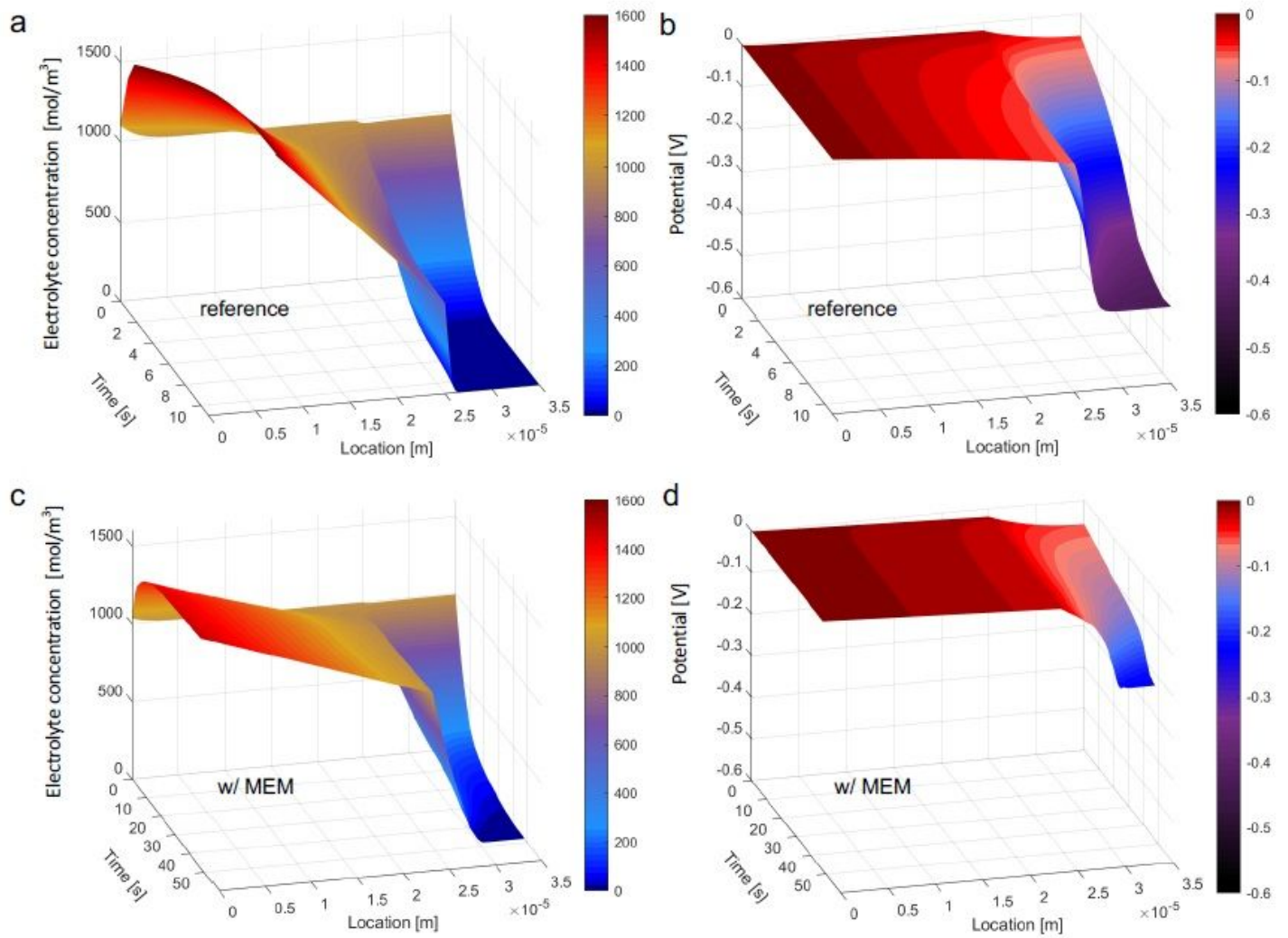


Figure 4

Polarization of electrolyte in simulated LiFePO₄|Li cells with and without MEM. (a, c) Simulated profiles of electrolyte concentration and (b, d) overpotential during discharging at a C rate of 50.

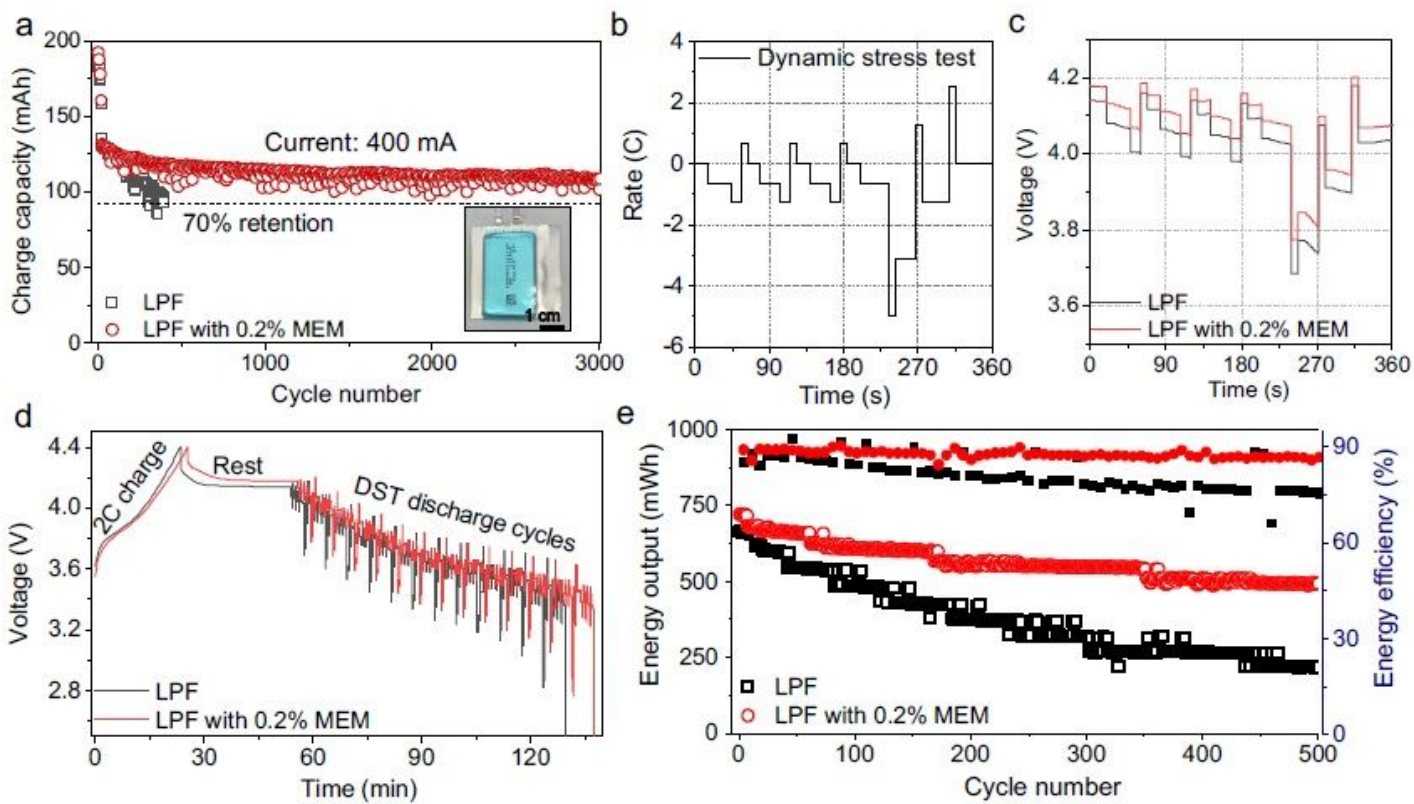


Figure 5

Performance of pouch cells with and without MEM in galvanostatic and dynamic stress tests. a, Galvanostatic cycling of commercial pouch cells at 400 mA and a voltage cutoff of 4.2 V (initial 10 cycles at 20, 30, 50, 100, 200 mA with 2 cycles for each rate). The inset shows photograph of a commercial pouch cell. b, Cycle protocol for a discharge process of the DST test. c, Voltage profiles of the first discharge segment of the DST. d, Voltage profiles for the first DST cycle. e, Cycling stability of pouch cells under DST.

Supplementary Files

This is a list of supplementary files associated with this preprint. Click to download.

- [MEMSI.pdf](#)
- [MEMSI.pdf](#)